applied sciences

MDPI

Article

Computational Investigation of the Factors That Affect Tangential Electric Fields along Cardiac Lead Paths inside MRI Birdcage Coils

George Tsanidis [1,2,*] and Theodoros Samaras [1,3]

[1] Department of Physics, Aristotle University of Thessaloniki, 54124 Thessaloniki, Greece; theosama@auth.gr
[2] Thessaloniki Software Solutions (THESS) S.A., Technopolis ICT Business Park, 55535 Thessaloniki, Greece
[3] Department of Physics, University of Malta, MSD 2080 Msida, Malta
* Correspondence: tsanidis@thess.com.gr

Featured Application: The existing literature has already examined the factors influencing power deposition at the tip of an active implant through in vitro or in silico studies on homogeneous phantoms and along their implantation pathways, which often do not correspond to real clinical scenarios. For this reason, a comparative study was conducted on six anatomically heterogeneous numerical models, where the electric field was calculated along 10,080 different paths of cardiac implantable electronic devices (CIEDs) and during 1140 different magnetic resonance imaging conditions. Beyond confirming several existing findings in the literature, paths of cardiac implants were identified that could lead to lower power deposition. It was also observed that a crucial parameter for determining the worst-case exposure of a patient with cardiac implants during MRI depends on the application of the IEC 60601-33 standard for patient safety.

Abstract: The medical imaging of a patient with a cardiac implantable electronic device (CIED) inside a magnetic resonance imaging (MRI) scanner carries the risk of tissue heating at the tip of the implant lead. In this work, we numerically assessed the impact of various factors, namely the resonant frequency, the imaging position, the implant position inside the human body and the coil configuration, on the induced tangential electric field along 10,080 cardiac lead paths at 1140 different scanning scenarios. During this comparative process, a function was considered based on the induced electrical potential at the tip of the lead. The input power of each coil was adjusted to generate constant $B_1{}^{+}{}_{RMS}$ at the iso-center or to limit the global SAR to the values provided in the safety guidelines IEC 60601-33. The values of the function were higher for higher static field and longer coil lengths when assessing the cases of a constrained $B_1{}^{+}{}_{RMS}$, and the trend was reversed considering the limiting SAR values. Moreover, the electric field was higher as the imaging landmark approached the thorax and the neck. It was also shown that both the choice regarding the insertion vein of the lead and the positioning of the implantable pulse generator (IPG) affected the induced tangential electric field along the paths. In particular, when the CIED lead was inserted into the left axillary vein instead of entering into the right subclavian vein, the electrical potential at the tip could be on average lower by 1.6 dB and 2.1 dB at 1.5 T and 3 T, respectively.

Keywords: cardiac lead; tangential electric field; coil configuration; imaging position; human body

check for updates

Citation: Tsanidis, G.; Samaras, T. Computational Investigation of the Factors That Affect Tangential Electric Fields along Cardiac Lead Paths inside MRI Birdcage Coils. *Appl. Sci.* **2024**, *14*, 786. https://doi.org/10.3390/app14020786

Academic Editor: Atsushi Mase

Received: 15 December 2023
Revised: 12 January 2024
Accepted: 15 January 2024
Published: 17 January 2024

1. Introduction

Magnetic resonance imaging (MRI) is a powerful and safe imaging technique in medical diagnostics. Nevertheless, the use of cardiac implantable electronic devices (CIEDs), both labeled and not labeled MR-conditional [1], inside MRI scanners has been studied experimentally both in terms of electromagnetic compatibility [2,3], as well as in terms of potential heating due to radiofrequency (RF) radiation. In particular, RF exposure can result in tissue heating in the vicinity of the implants at the tips of leads of active implantable medical devices (AIMDs), where electrodes are located [4]. However, it is estimated that more than 50% of patients with implanted medical devices will require an MRI exam during their lifetime [5]. Therefore, many previous studies reported in vitro measurements of the induced heating at the tip of a pacemaker implant [6,7] and in vivo measurements [8] for specific electrodes, MRI systems and conditions.

In addition, previous works have studied several factors that influence the amount of heating at the lead tip, such as the lead geometry [9,10], the conductivity of the medium at the lead tip [11,12], the location of the implant inside the body [13], the coil [14,15] and the MR systems [16,17]. In these studies, temperature measurements were evaluated in homogenous phantoms in 1.5 T coils, and, in the majority of the cases, the lead configurations did not reflect realistic clinical scenarios since the positioning of the device inside a phantom cannot reproduce specific clinical pathways.

Therefore, because of the high degree of complexity during the interaction between the MRI coil and the implant, the results of previous works measured in homogenous phantoms might not provide enough confidence regarding patients' safety as the patient's body composition alters the RF power deposition in the tissue surrounding implanted leads [18–23]. In [24], the RF-induced electric field inside a homogenous phantom was assessed, demonstrating a different spatial distribution compared to the respective distribution inside a human model [25]. In addition, in [26], the induced E-fields along paths of typical implants inside patient models were compared to those induced in the ASTM phantom and it was concluded that the phantom was not always conservative relative to clinical exposures. Furthermore, ref. [27] presented a database of MRI-induced heating measurements quantifying the contributions of the above factors showing in addition that the temperature increase inside a human-shaped phantom was lower than in a rectangular model, emphasizing the effect of the morphological properties of a model in addition to the properties of its material.

Regarding the impact of the imaging landmark on the risk of unintended implant heating, in [24], it was demonstrated that the induced electric fields inside the body shifted when the body positioning was changed, and, in [28], less absorbed RF energy was calculated at an external fixation device when it was moved out of the coil. Similarly, in [22], it was shown that imaging positions around the lower sternum and the abdomen of non-homogenous numerical models tend to have higher induced electric fields inside the body.

Moreover, in previous works, RF heating during MRI was reduced, modifying the trajectories of Deep Brain Stimulation (DBS) leads inside homogenous phantoms [29,30], and in [31] it was concluded that the surgical modification of epicardial lead trajectory can substantially reduce RF heating at 1.5 T. On the other hand, although for endocardial CIED implantation the leads are placed through the subclavian vein and the implantable pulse generator (IPG) is consistently placed in the subclavian pocket, resulting in limited variation in their trajectories, in [32], it was noticed that differences in RF heating existed between various implantation paths inside anthropomorphic homogenous phantoms.

The majority of previous studies focused on the 1.5 T coil, although 3 T MRI scanners are becoming more common in clinical practice as they show improved diagnostic accuracy and shorter procedure times [33]. The significant increase in local SAR (Specific Absorption Rate) for a given imaging sequence, the shorter RF wavelengths and the different RF field distribution in coils with higher static field strengths add another layer of complexity in heating patterns [34]. However, in [35], it was concluded that coils at higher resonant frequency performing a conservative safety criterion, such as the global SAR, tend to generate lower local SAR around implanted leads.

The relevant safety guidance is IEC 60601-33 [36], with the guidelines suggesting maximum levels of SAR that limit RF heating in patients during MRI; these guidelines are used in MRI systems [37] and by most implant manufacturers to assess the safety of their product. The commercial MRI systems provide an estimation of the SAR based on the RF waveforms and sequence parameters, coil factors and anatomical properties of the patient with high uncertainty on the reliably estimation of SAR. Therefore, different metrics have been considered, such as the $B_1{}^+{}_{RMS}$ value at the iso-center of the coil.

In summary, while a series of prior works have focused on the contribution of imaging conditions to induced heating at the tip of an implant, these were primarily conducted using measurements and numerical methods on homogeneous phantoms, with implant placements that did not correspond to real clinical scenarios. Moreover, these studies did not concentrate on cardiac implants and did not cover all the possible conditions (resonant frequency, landmark and coil configuration). Consequently, the present study addresses the gaps in the previous research, and its main contributions can be outlined as follows:

(1) For the first time, a comparative estimation of the induced tangential electric field along CIED leads is performed on a large dataset corresponding to real clinical scenarios. Specifically, cardiac implant paths were designed within six human anatomical models considering ten different landmarks (imaging positions) within ten characteristic configurations of 1.5 T and 3 T birdcage coils, resulting in 1,843,200 different cases of incident electric fields. In order for the results to be reliable and qualified, human models and birdcage coils accepted by the FDA (Food and Drug Administration) as Medical Device Development Tools (MDDTs) were used.

(2) For each birdcage, landmark and model, the induced electric field was scaled to a constant $B_1{}^+{}_{RMS}$ value at the iso-center or to the corresponding SAR limits of the Normal Operating Mode of the MRI [36], aiming to identify the worst-case scenario. This aspect was not clarified by ISO TS 10974 [38] during the process of characterization of an implant as MRI-safe.

(3) Efforts were undertaken to identify the imaging conditions and cardiac paths with the least significant effect on tissue heating within numerical human models of detailed anatomy. This could lead to the development of an additional safety margin for a patient's safety during MRI, either during imaging or even during a surgical procedure of implant placement by the physician.

2. Materials and Methods

2.1. Virtual Population and Birdcage Coils

Since the induced fields in the human body are a function of multiple variables like the birdcage geometry, the anatomy of the model and the imaging landmark position [39], 1140 different clinical scanning scenarios were assessed. In particular, four adult anatomical models (Duke, Ella, Glenn and Fats) and two children models (Louis and Billie) from the Virtual Population (ViP version 3.1, IT'IS Foundation, Zurich, Switzerland) were used to evaluate a wide range of model variability [40]. Their morphological characteristics are included in Table 1. The tissue properties for both 1.5 T and 3 T were assigned according to the IT'IS Foundation database (version 3.0) [41].

Table 1. Morphological characteristics of the used Virtual Population numerical models.

Model Name	Sex	Age [Years]	Height [m]	Weight [kg]	BMI [kg/m^2]	No. of Tissues
Duke	M	34	1.77	72.4	23.1	77
Ella	F	26	1.63	58.7	22.0	76
Billie	F	11	1.47	35.4	16.5	75
Louis	M	14	1.69	50.4	17.7	77
Glenn	M	84	1.73	65.0	21.7	84
Fats	M	37	1.82	119.6	36.2	79

The models were placed inside 10 different cylindrical RF birdcage body coils from the Birdcage Library (BCLib, IT'IS Foundation, Zurich, Switzerland) with different dimensions as shown in Table 2. The resonant frequencies of the coils were set to 64 MHz for the 1.5 T system and 128 MHz for the 3 T system. Clockwise polarization was assumed, implementing a quadrature excitation by feeding the coils with two ports 90° apart in azimuth (polar) angle and phase. For each model, 10 different landmarks (LD_1–LD_{10}) were considered, with a 10 cm step from head to feet, where the center of the heart was kept on the craniocaudal axis (z-axis). The first landmark coincided with the RF-coil iso-center 10 cm below the head imaging position, as shown in Figure 1. In Table 3, the evaluated landmarks are matched to usual clinical imaging positions. In order to decrease the computational burden, a Huygens source was used, which was constructed from the field distribution provided by the birdcage coils of the BCLib, and uniform isotropic voxel size was assigned at the human models with a resolution of 2 mm. Full-wave electromagnetic simulations were performed until steady state was reached. Varying the number of the simulated periods from 7 to 15 was tested for convergence of the results; after 8 simulation periods, the deviation in the results was negligible. In particular, the deviation in the maximum electric field was less than 0.05%.

Table 2. Physical dimensions of the cylindrical RF (birdcages) coils.

Coil Name	Bore Size (cm)	Coil Inner Diameter (cm)	Coil Length (cm)	Shield Inner Diameter (cm)
Coil 1	60	70	50	70
Coil 2	60	70	60	70
Coil 3	60	70	70	70
Coil 4	70	75	40	80
Coil 5	70	75	50	80
Coil 6	70	75	60	80
Coil 7	70	75	70	85
Coil 8	75	80	50	85
Coil 9	75	80	60	85
Coil 10	75	80	70	85

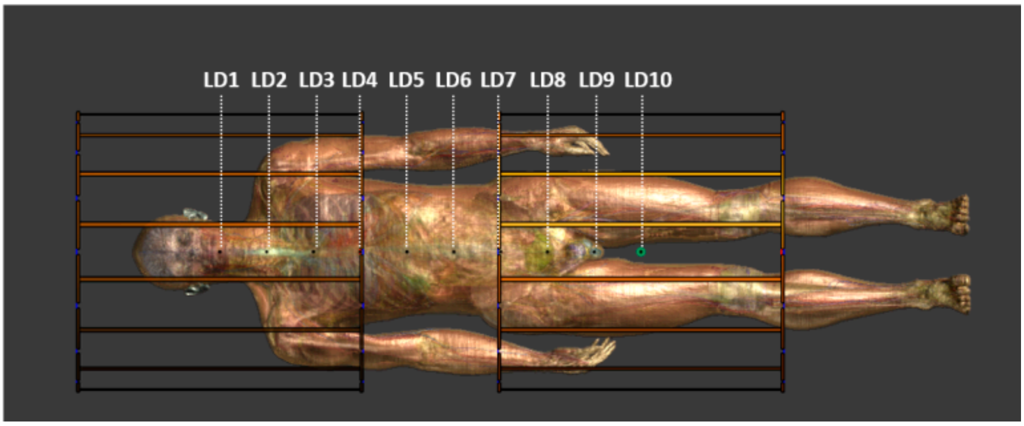

Figure 1. Definition of the ten different positions of the coil iso-center.

Table 3. Matching of imaging positions with the 10 different landmarks.

Landmarks	Imaging Position
LD_1 LD_2	Head and neck
LD_3 LD_4	Thorax
LD_5 LD_6	Lumbar
LD_7 LD_8 LD_9 LD_{10}	Pelvis

2.2. Lead Implantation Paths

Based on the clinically relevant implantation paths as described in [42], the lead paths were terminated inside the heart at three different points, at the right atrium (point P_1), at the septum wall (point P_2) and at the apex of the right atrium (point P_3), as shown in Figure 2. Then, the paths followed the superior vena cava to the subclavian vein and exited from the veins from three different possible points, the subclavian vein (point V_1), the cephalic vein (point V_2) and the axillary vein (point V_3), respectively. This approach was followed for both the right and the left side of every human model, as depicted in Figure 3.

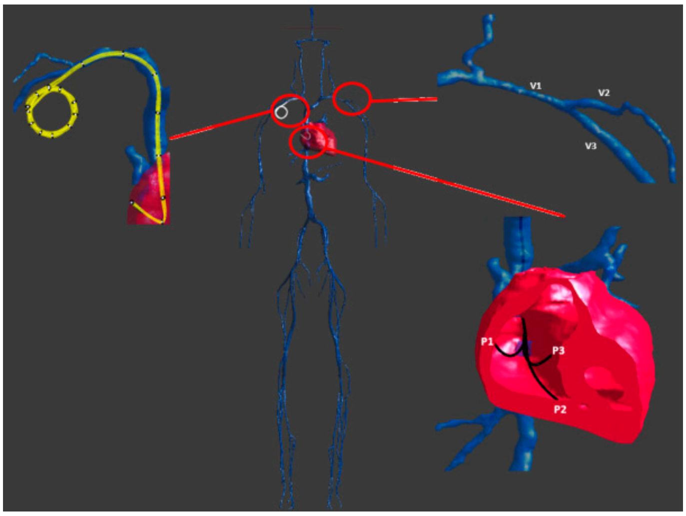

Figure 2. The termination points inside the heart (P1, P2, P3), the vein exit points (V1, V2, V3) and the 40 random splines.

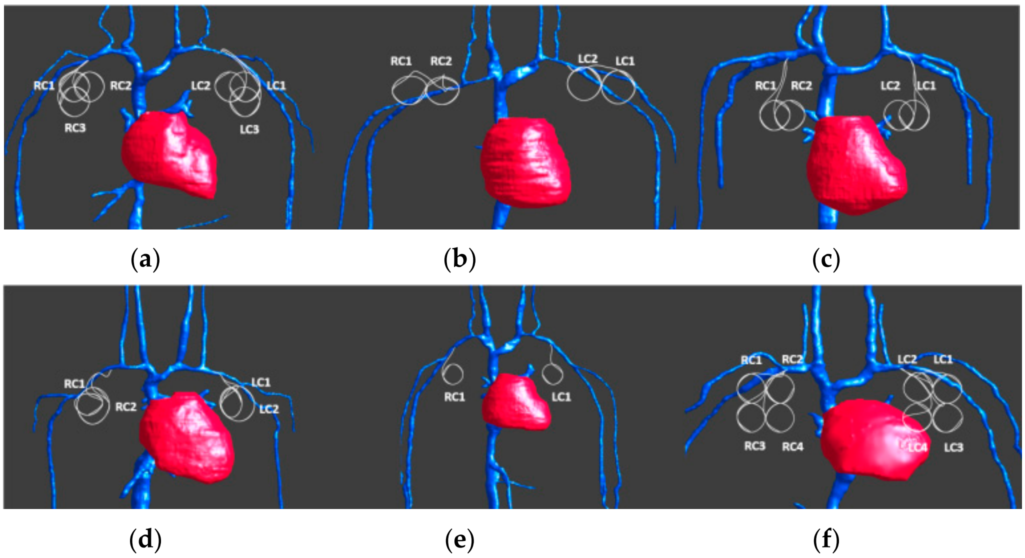

Figure 3. The implantation paths in the numerical models of Duke (**a**), Ella (**b**), Glenn (**c**), Louis (**d**), Billie (**e**) and Fats (**f**).

After exiting from the veins, the paths were terminated at the pectoral regions, at points where a connection of the lead to the IPG was assumed. However, the remaining part of the lead that left the vein was coiled before connecting to the IPG. The coiling of the lead was performed with two constraints, i.e., the flexibility of the lead (minimum allowed radius of curvature) and the subcutaneous space available inside the body (numerical phantom). In the present study, the coiling circles were chosen with a diameter between 40 and 60 mm. However, it was not possible to create the same number of different coiling circles in every human model or in either side of the same human model due to their anatomical characteristics. The total number of implantation paths that were identified in each human model (which are illustrated in Figure 3) is provided in Table 4. This number includes all cases: left- and right-side implantation, entrance of the lead through the subclavian, cephalic and axillary veins.

Table 4. Number of coiling circles and possible implantation paths per anatomical model.

Model Name	No. of Coiling Circles	No. of Potential Implantation Paths
Duke	3	54
Ella	2	36
Billie	1	18
Louis	2	36
Glenn	2	36
Fats	4	72

Around each of the potential implantation paths, 40 random splines (trajectories) were created with the use of the IMSAFE tool, embedded inside the Sim4Life computational platform (ZMT, Zurich, Switzerland), as shown in Figure 2. These splines were created inside tubular spaces formed by successive cylindrical disks with a radius of less than or equal to 5 mm so that they never crossed outside the vein walls anywhere else but at the entry and exit points. Then, the tangential electric field components were extracted along the splines and were averaged (magnitude and phase) every 5 mm. Therefore, taking into account the 6 human models, the 10 imaging positions and coil configurations, as well as the 2 resonant frequencies, 1,843,200 paths were considered for the evaluation of the tangential electric field and the corresponding impact of every factor mentioned above.

2.3. Calculation of the Power Deposition at the Tip of the Implant

The determination of the temperature rise in the tissues caused by AIMDs during an MRI session is described in ISO TS 10974:2018 [38]. A four-tier approach has been elaborated with increased complexity and accuracy of estimation between successive tiers. The lower tiers are based on simplifications of the exposure situation, yielding an overestimation of the temperature increase and, therefore, a larger safety margin. On the contrary, the higher tiers involve the realistic implant placement of AIMDs in the human body and the accurate calculation of the incident fields, reducing the overestimation and resulting in a more realistic prediction of the temperature rise.

In particular, the Tier 3 approach uses the concept of the transfer function (TF) of an implant and relates the incident tangential electric field along a path to the deposited power in the tissue surrounding the lead tip, which leads to temperature increase [43]. The Tier 4 approach combines the use of anatomical human models and detailed modelling of the implants, thus resulting in the least overestimation compared to the in vivo exposure. However, the simulation time and, in general, the computational resources for the latter evaluation are highly demanding.

According to the transfer function approach, the power deposition at the tip of the implant is provided by

$$P = A\left(\int_L E_{tan}(z)S(z)dz\right)^2 \quad (1)$$

where S(z) is the transfer function (TF), A is a calibration factor and E_{tan} (z) is the tangential component of the incident electric field along the lead pathway inside the patient, without the lead in place. Hence, the TF decouples the scattered field from the incident, simplifying the computation.

The aim of this work was not to calculate the absolute values of the deposited power at the tip of the lead but to compare among the different pacemaker paths inside a human model under different scanning scenarios independent of the structure of the device. Thus, the square of the excitation potential across the different paths was assessed as provided by

$$W = \left| \int_L E_{tan}(z)dz \right|^2 \quad (2)$$

which is proportional to the temperature increase at the tip, as demonstrated in [44]. Equations (1) and (2) are equal for a unity transfer function S(z). Similar approaches have been used in previous works for the assessment of the impact of a high dielectric material at the tip of the implant [45,46] or for the results of the different positions of the feeding sources on an RF coil [47]. The tangential electric field was scaled to the SAR limits of the Normal Operating Mode as defined in safety standard IEC 60601-2-33 [36]. In particular, regarding the landmarks LD_1 and LD_2, the limit of the head-averaged SAR (3.2 W/kg) was assessed and, for the rest imaging positions, the limit of the whole body averaged SAR (2 W/kg) was used. As many commercial CIEDs are labeled as MR-safe for specific maximum allowed B_1^+ field, the electric field was also scaled to the value of 2 μT at the iso-center of the coil. Both outcomes were chosen because they are automatically calculated and reported by a scanner and are commonly adopted in MRI conditional guidelines and labeling of devices [35].

Thus, the estimation of the normalized W values along potential trajectories of cardiac implants was performed after separating them according to the patient's side of termination (right or left), and their distribution was studied, along with their mean value, in relation to the landmark of each human model and coil configuration. These values were further stratified based on the entry point into the vein as well as the termination point within the heart to investigate the impact of implant placement in the patient. Additionally, to determine the effect of the resonant frequency of each birdcage coil, a comparison was made between these values as derived from each trajectory at 64 MHz and their corresponding values at 128 MHz.

3. Results

3.1. Results at 1.5 T

The investigation of the extracted tangential electric field along the paths of CIEDs inside the model of Duke at 1.5 T are shown in Figure 4, where the W values were separated for pathways leading to the right side of the patient from those leading to the left placement of the IPG device. The distribution inside the rest of the models is provided in the Supplementary Materials (Figure S1). In particular, the distribution of the W values over all the imaging positions is presented, where the input power of the coil was adjusted to generate $B_1^+{}_{RMS}$ = 2 μT at the iso-center (Figure 4a) or to assess the limiting value of the global SAR (Figure 4b). The dotted lines present the mean values of the W values. The most unfavorable scenario (with the highest mean W value) at 1.5 T, assuming a constant $B_1^+{}_{RMS}$ at the coil's iso-center, occurred during thoracic imaging (LD_3). Conversely, when fixed SAR was taken into account, the highest electric field was estimated during neck imaging. For both approaches, the electric field along the cardiac paths decreases with moving the human away from the center of the coil. Therefore, the selection of the appropriate imaging landmark is a dominant factor for reducing the deposition of the RF power at the tip of a CIED. Tables S1 and S2 in the Supplementary Materials summarize this obtained reduction in dB of the mean W value for each landmark relative to the worst case, where, at the low part of the lumbar and at the pelvis, the electric field reduced by more than 10 dB.

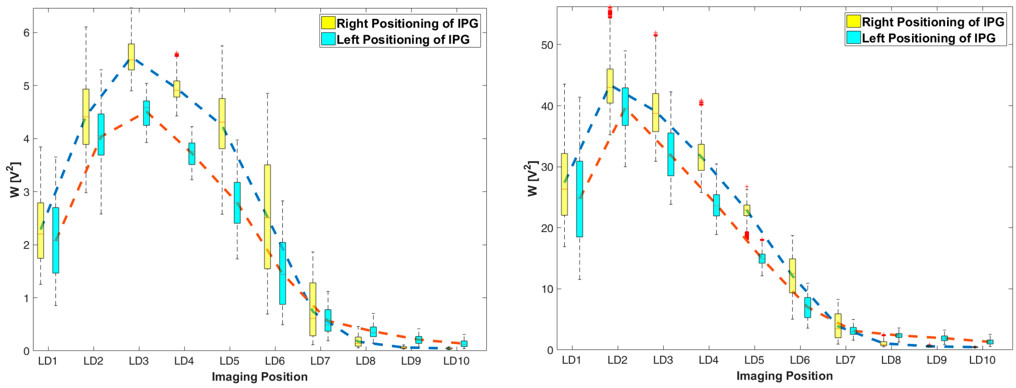

(**a**) (**b**)

Figure 4. Distribution of the magnitude of the tangential electric field at 64 MHz inside the Duke model over all imaging positions. The input power of the coil was adjusted to generate (**a**) $B_1{}^+{}_{RMS}$ = 2 µT at the iso-center and (**b**) the limiting value of the global SAR. The blue and the red dotted lines present the mean values of W for the right and left positioning of the IPG, respectively.

Furthermore, Figure 5 displays the impact of the coil's dimensions on the extracted electric field at the position LD_3 for both considerations. The deviation in dB for each configuration relative to the worst case (highest mean W value) is provided in Tables S3 and S4 in the Supplementary Materials. The values of electric field scaled to constant $B_1{}^+{}_{RMS}$ at the iso-center were always higher for longer coils, whereas, when they were scaled to the limiting values of SAR, they were higher for shorter coils.

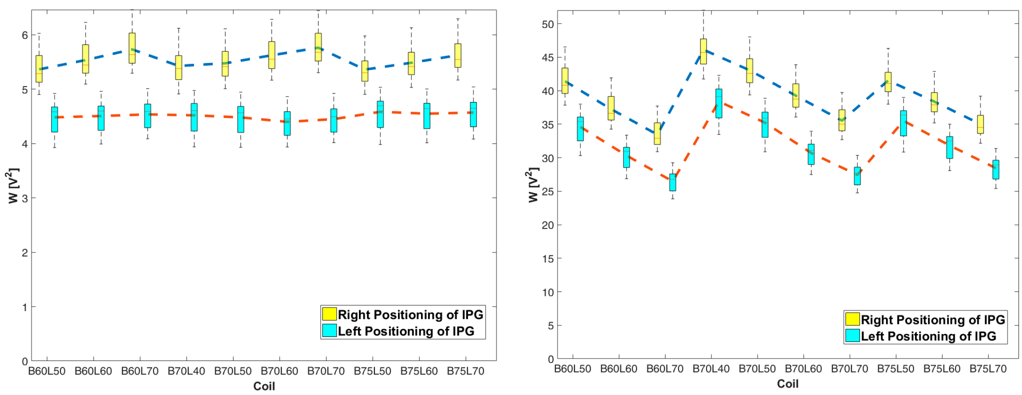

(**a**) (**b**)

Figure 5. Distribution of the magnitude of the tangential electric field at 64 MHz inside the Duke model over all the coil configurations at landmark LD_3. The input power of the coil was adjusted to generate (**a**) $B_1{}^+{}_{RMS}$ = 2 µT at the iso-center and (**b**) the limiting value of the global SAR. The blue and the red dotted lines present the mean values of W for the right and left positioning of the IPG, respectively.

3.2. Results at 3T

The results of the electric field along the paths of CIEDs at 3T versus the imaging position and the coil configuration are shown in Figures 6 and 7. Similar to the results shown at 1.5 T, the landmark position affected the distribution of the electric field, and values lower than 10 dB occurred for imaging the region of the lumbar and pelvis in comparison to the imaging of the thorax, as is also presented in Tables S1 and S2. As is also shown in Tables S3 and S4, the highest electric field corresponded to different coil height depending on the considered exposure limits.

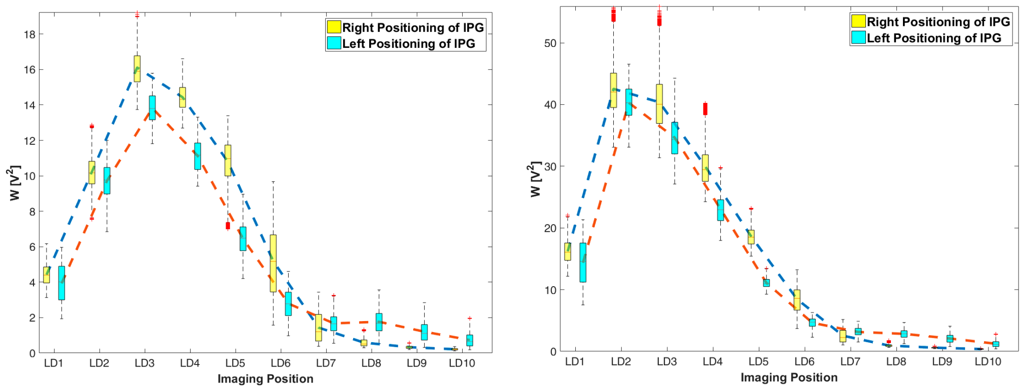

(**a**) (**b**)

Figure 6. Distribution of the magnitude of the tangential electric field at 128 MHz inside the Duke model over all imaging positions. The input power of the coil was adjusted to generate (**a**) $B_1{}^{+}{}_{RMS}$ = 2 µT at the iso-center and (**b**) the limiting value of the global SAR. The blue and the red dotted lines present the mean values of W for the right and left positioning of the IPG, respectively.

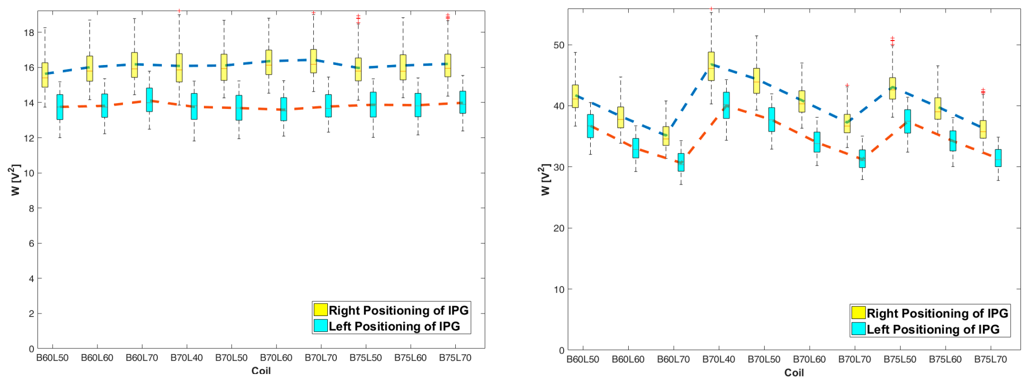

(**a**) (**b**)

Figure 7. Distribution of the magnitude of the tangential electric field at 128 MHz inside the Duke model over the dimensions of the coils at landmark LD3. The input power of the coil was adjusted to generate (**a**) $B_1{}^{+}{}_{RMS}$ = 2 µT at the iso-center and (**b**) the limiting value of the global SAR. The blue and the red dotted lines present the mean values of W for the right and left positioning of the IPG, respectively.

3.3. Impact of Frequency

Regarding the impact of the resonant frequency on the induced electric field, the scatter plots in Figure 8 present the correlation of the W values for each path of the CIEDs inside the model of Duke, at LD_3, as were estimated at 1.5 T and 3 T. When the power of each coil was adjusted to generate $B_1{}^{+}{}_{RMS}$ = 2 µT at the center of the coil, the electric field was significantly lower at 1.5 T than that at 3 T (Figure 8a), while, for the SAR fixed at the normal operation limiting values, the difference between the results of the two resonant frequencies was much lower. Figure 9 displays the resulting distribution in dB of the deviation between the electric field at both resonant frequencies for all numerical models. Assuming constant $B_1{}^{+}{}_{RMS}$, the electric field was higher at 3 T along the cardiac paths than at 1.5 T from 1.5 to 5.7 dB. On the other hand, fixing SAR resulted in differences in the range of −1.7 to 1.6 dB, demonstrating that there are paths with a higher induced electric field at 64 MHz than at 128 MHz.

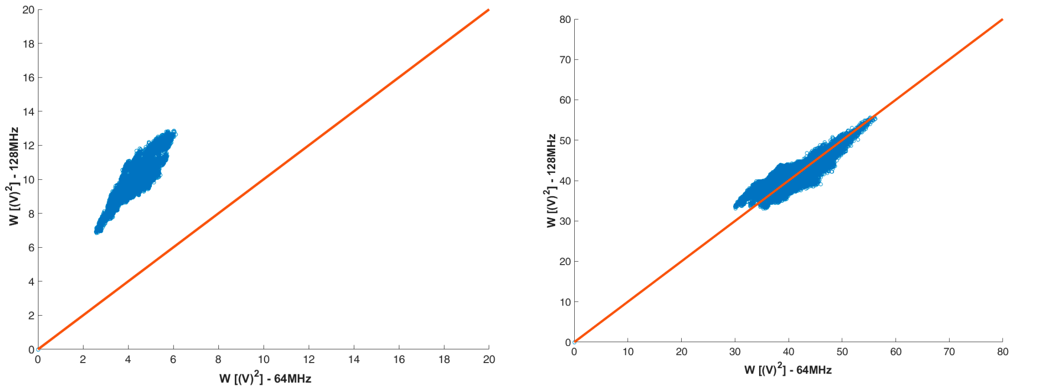

(**a**) (**b**)

Figure 8. Scatter plot of the magnitude of the tangential electric field inside the Duke model correlating the W values at 1.5 T to the corresponding ones at 3 T. The input power of the coil was adjusted to generate (**a**) $B_1{}^+{}_{RMS}$ = 2 μT at the iso-center and (**b**) limiting value of the global SAR. The red solid line corresponds to the equivalence of the two quantities.

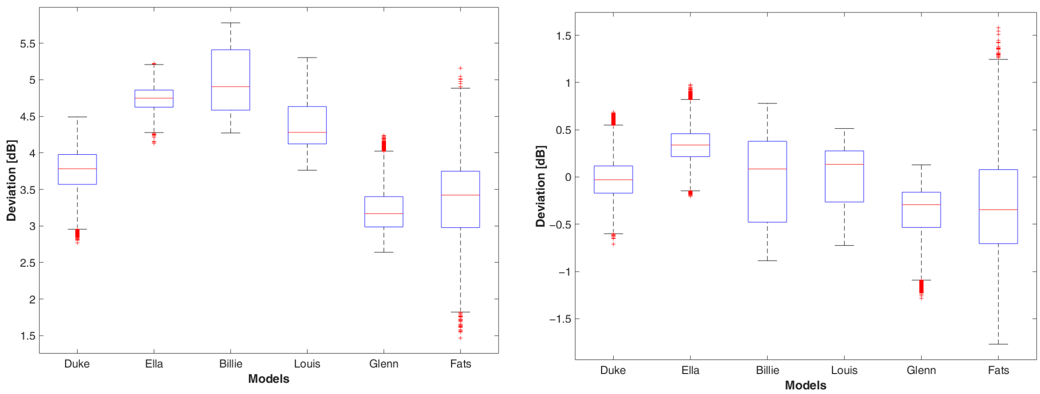

(**a**) (**b**)

Figure 9. Distribution of the deviation in dB between the tangential electric fields at 1.5 T and 3 T over all the numerical models. The input power of the coil was adjusted to generate (**a**) $B_1{}^+{}_{RMS}$ = 2 μT at the iso-center and (**b**) the limiting value of the global SAR.

3.4. Impact of Pacing Lead Positioning Inside the Body

In several previous studies, where temperature measurements in phantoms [9,13,27] and animals [8] were performed or the temperature was numerically calculated [30], it was reported that the temperature rise was significantly higher when the IPG was positioned in the right pectoral region in a 1.5 T MR system. In this study, these data were confirmed and the numerical deviation between the left and right pectoral region was evaluated. Figure 10 shows scatter plots of the estimated W values inside Duke, separating the right and the left side of the anatomical models landmarked at the heart (LD_3) for both resonant frequencies and all coil configurations. In particular, each point correlates the extracted electric field along paths that started from the same point and finished at the right or the left side of the patient (e.g., P_1-V_1-RC_1 vs. P_1-V_1-LC_1). Table 5 summarizes the deviation (in dB) between the mean W values over all the paths leading to the right positioning of IPG versus the left placement.

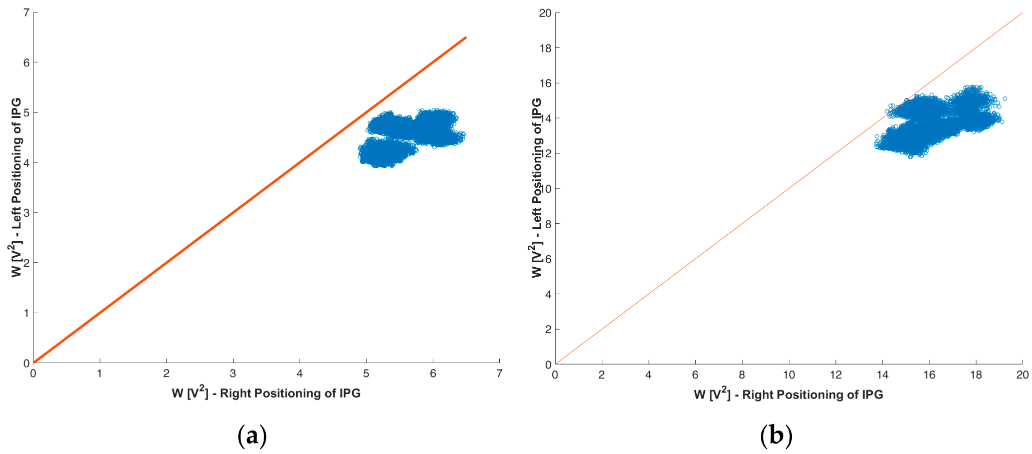

Figure 10. Scatter plot of the W values of the left placement of the IPG versus the right placement (**a**) at 1.5 T and (**b**) at 3 T. The red solid line corresponds to the equivalence of the two quantities.

Table 5. Increase in the electric field (in dB) at the right positioning of IPG versus the left one.

Model Name	MRI System	
	1.5 T	**3 T**
Duke	0.8	0.6
Ella	0.3	0.2
Billie	0.4	1.3
Louis	0.4	0.9
Glenn	1.9	2.2
Fats	2.2	1.7

Furthermore, to associate the energy absorption at the implant tip with the location of the lead inside the human model, the estimated W values over all the coil configurations and imaging landmarks were grouped according to the veins where the lead paths were inserted, and the results are summarized in Figure 11 for both frequencies. Both right and left routes were considered, and the results correspond to the landmark LD_3. In most of the human models, the highest calculated electric field was achieved along the subclavian vein, while the relative minimum was observed along the axillary vein. For both right and left paths and both resonant frequencies, the mean W value was found to be lower at paths inserting from the axillary vein than those from the subclavian vein, by 0.4–0.7 dB.

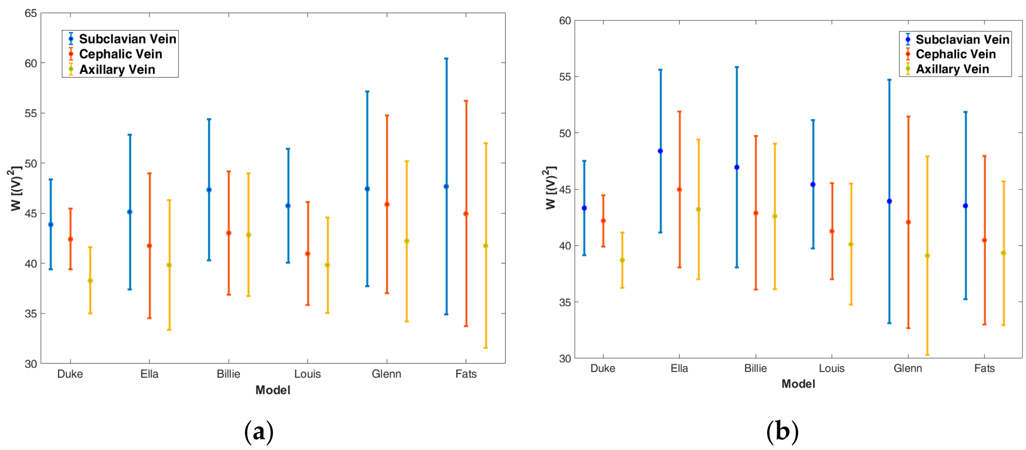

Figure 11. Distribution of the W values for all numerical models regarding the insertion point of the paths (**a**) at 1.5 T and (**b**) at 3 T.

Finally, the results were grouped based on the termination point inside the heart (points P_1, P_2 and P_3) and are shown in Figure 12. It can be seen that the impact of the route inside the heart on the total deposited power was dependent on the anatomy of the human model.

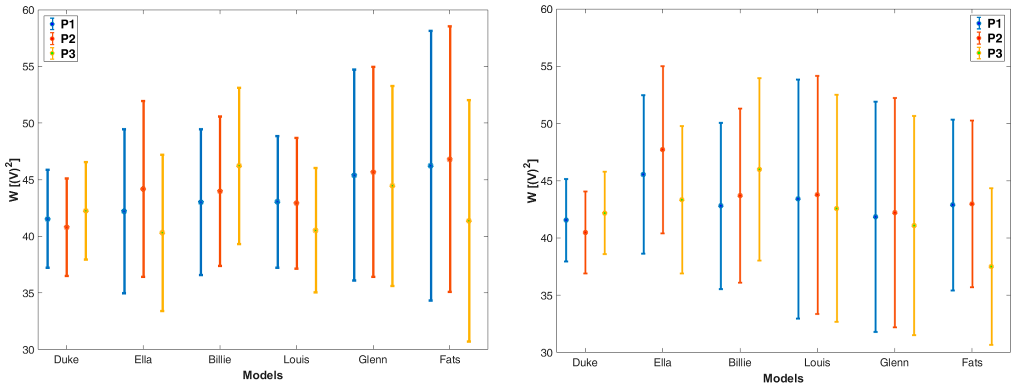

(**a**) (**b**)

Figure 12. Distribution of the W values for all numerical models regarding the terminating points of the paths inside the heart at (**a**) 1.5 T and (**b**) 3 T.

4. Discussion

In previous publications, it has been shown that many factors affect the heating of an implant tip, namely the implant's position inside the human body, the imaging landmark and the type of coil system. Therefore, in order to find simple and practical methods to control the induced RF heating close to the CIEDs, the influence of these factors on the induced tangential electric field along cardiac leads was estimated numerically. As the safety guidelines offer the option to cap either the global SAR or the $B_1^+{}_{RMS}$, which are both automatically calculated and reported by the scanners, we conducted a systematic comparative study of these impact factors on the induced electric field considering the limitations of IEC 60601-2-33 [36].

As was shown in previous works, the body positioning inside the scanner affects the distribution of the tangential electric field along the leads and therefore the absorbed energy at the implant tip, determining the neck and the thorax imaging landmarks as the worst imaging zone. In particular, assuming constant $B_1^+{}_{RMS}$, at both frequencies, the peak values were obtained at the level of the heart (LD_3) and at the high part of the chest (LD_4), followed by the landmarks at the low part of the chest and the neck. On the other hand, considering constant global SAR, higher W values were estimated for most of the human bodies at the landmark of the neck (LD_2). Therefore, although the central position of an implant is suggested to generate the maximum heating [8], the consideration of the limits could affect this. For both limitations, the pelvis imaging position could be characterized as a safety zone for the cardiac leads since the calculated W values were decreased by more than 10 dB compared to the maximum, ensuring highly reduced deposition of the energy. This was also confirmed in previous studies [14,25,26,48].

Furthermore, it was noticed that the obtained reduction in the electric field removing the imaging position from the worst-case landmark depended on the dimensions of the coil. In particular, the length of the birdcage coil seemed to influence the induced electric field along the paths, whereas the change in the radius of the bore resulted in negligible differences. Therefore, considering constant $B_1^+{}_{RMS}$ at the iso-center, the W values were higher as the length of the coil was longer. On the other side, assessing constant global SAR inside the shorter birdcage coils led to higher W values than the rest of the coils.

Although it is expected that an increase in the magnetic field strength affects implant heating, it is observed that this mainly depends on the enforcement of the IEC 60601-2-33 limitations [36]. This discrepancy is explained by the constant global SAR over the resonant frequencies, leading to lower B_1^+ magnitude at higher resonant frequencies and subsequently to lower electric field, which is in line with previous work [46]. On the other hand, the constant $B_1{}^{+}{}_{RMS}$ value generates higher electric field at higher resonant frequency. This is in agreement with previous studies that compared the RF heating of DBS implants across 1.5 T and 3 T coils [30,47]. The difference in the resonant frequency of the coil implies an increase in the induced potential on a lead by 1.7 to 5.7 dB at 128 MHz in comparison to 64 MHz for the same $B_1{}^{+}$. The obtained increase is close to the value reported in previous studies, where the SAR rose quadratically with B_0, increasing by 6 dB [49]. Nevertheless, it is important to note that the estimated factor characterizes the contribution to the final RF-induced power deposition of the electric field only and not to the TF, which also varies by changing the applied frequency and the electric length, which is a key parameter for the coupling mechanism between the coil and the implant.

In summary, the consideration of limiting SAR led to a different distribution of the W values in comparison to those of limiting the $B_1{}^{+}{}_{RMS}$. The reason is that the higher resonant frequency, the imaging position close to the thorax and the longer coils generally tend to generate higher induced local SAR, and thus the electric field was scaled to lower values to maintain compliance with the limiting values. This appears to be in accordance with a previous study [26]. Therefore, this numerical analysis of the induced electric field along cardiac implants under different imaging scenarios revealed conflicts among different versions of the IEC 60601-2-33 standard. Specifically, in the 2015 edition, the determination of normal mode (NM) and first-level controlled mode of operation for a magnetic resonance imaging (MRI) system introduced the FPO:B (Fixed Parameter Option: Basic) choice. This option sets safety limits under specific patient exposure conditions. This addition essentially ensures that, during MRI operation, by applying fixed parameters, the patient's safety limits are maintained. However, in this study, for the first time, it was observed that, during the Tier 3 process, the application of different options of the standard results in a different distribution of the induced electric field and consequently the calculated absorbed power. This does not always make the FPO:B approach more conservative. This highlights the need to adopt both options of the IEC 60601-2-33 standard in the Tier 3 process to compare results and consider the most adverse patient radiation condition. Thus, the necessity arises to include this specific condition not covered in existing versions of ISO TS 10974.

Apart from the impact of the imaging position and the coil configuration on the deposited energy, the effect of the implant path inside the human body was also evaluated, indicating some paths that consistently reduced the RF deposited power over different resonant frequencies, human models and imaging landmarks. In particular, the induced W values for the leads implanted along the axillary vein were lower by 0.4 to 0.7 dB than the corresponding ones along the subclavian vein. On the other hand, the effect of the terminating point inside the heart was found to depend on the anatomy of the human model. Moreover, the excited W on the left side trajectories was lower by 0.2 to 2.2 dB than the corresponding one on the right side of the imaging position LD_3 for both 64 and 128 MHz The reason for this right–left asymmetry is the clockwise polarization of the MRI, which for the supine position of the patient leads to a higher electric field at the posterior right edge and at the anterior left edge than estimated in previous works [15,50]. Therefore, an additional margin of safety could be achieved for patients with CIEDs undergoing MRI procedures for both 1.5 T and 3 T systems by considering the path of the lead. In particular, when the cardiac lead inserts into the left axillary vein instead of the right subclavian vein, the deposited power at the tip of a pacemaker could be on average lower by 1.6 and 2.1 dB at 64 and 128 MHz, respectively. This is an observation that has not been reported before and has not been exploited in clinical practice until now.

In previous works, the main goal was the reduction in the localized heating in patients with implants by modifying the device to reduce the coupling with the electric field [10,44,47] or by monitoring the induced current [13,51,52], even by modifying the RF coil [43,53–55]. However, the above-mentioned approaches are not compatible with the existing implants and birdcage coils as they are applied after the implantation of the device. Hence, based on the analysis of the factors affecting the induced power on a pacemaker, we propose a more appropriate solution based on varying the placement of the device inside the human body. Therefore, from a practical perspective, optimal cardiac paths could be implemented in patients with minimum disruption to surgical flow, improving safety issues without added cost. It should further be noted that lead trajectories that reduce RF heating could also reduce image artifact as it is caused by induced currents, which are responsible for tissue heating and for production of the secondary magnetic fields that distort the B_1 field [56].

The entire applied process relied on electromagnetic simulations, and, recently, in order to avoid the required computational time and memory requirements, novel machine learning methods have been proposed for the assessment of MRI RF heating. Specifically, the application of neural networks has been proposed to predict the worst-case heating of orthopedic fixation plates in the MRI environment, with the only input being the geometric properties of the implant [57]. Additionally, deep learning has been applied to predict the SAR values at the tip of conductive leads along clinically relevant cardiac and DBS paths during 1.5 T and 3 T MRI [58–60]. This achieves a fast method for estimating the safety of patients with only knowledge of the lead's geometry and MRI RF coil features, enabling the study of the impact of the implant's placement and imaging conditions. Nevertheless, this methodology is constrained to homogeneous human models, leading to variations in the predicted electric field compared to its actual counterpart within the human body.

This work has several limitations. Initially, the investigated paths refer to CIEDs, such as pacemakers (PMs), implantable cardioverter defibrillators (ICDs) and cardiac resynchronization therapy (CRT) devices, for which the transvenous implantation is used (endocardial systems). Therefore, this work does not include epicardial systems, which are stitched directly to the myocardium and connected to an IPG placed in the abdomen. Moreover, the extracted electric fields along the paths were normalized to an established safety limit (SAR or $B_1^+{}_{RMS}$) intended for implant-free patients and not always suited for patients with implants [50]. Another limitation of our study is that it focused on the induced electric field along the cardiac paths considering the different dielectric properties of the tissues surrounding the implanted devices without calculating the subsequent RF heating. Since the different thermal properties of tissues could induce high temperatures even in tissues with low deposited power, complimentary work is required. Furthermore, since the values of electric fields within the six anatomical models varied widely due to their different morphological and anatomical characteristics, and as local quantities can vary more than 10 dB depending on the anatomy [61], studying a larger number of models could cover the patient population in any safety evaluation.

5. Conclusions

A comparative estimation of the induced tangential electric field was investigated along 10,080 CIED leads at 1140 different scanning scenarios considering various implant placements inside six human anatomical models, within ten characteristic configurations of 1.5 T and 3 T birdcage coils, at ten different landmarks. The highest electric field depended not only on the imaging position, the resonant frequency and the coil configuration but also on the limitation imposed to avoid partial- or whole-body heating of the patient during an MRI scan. Finally, the study indicates the prospect of a significant reduction in the deposited power at the tip of the implant by proposing a lead management strategy.

Supplementary Materials: The following supporting information can be downloaded at: https://www.mdpi.com/article/10.3390/app14020786/s1, Figure S1: Distribution of the magnitude of the tangential electrical field at 64 MHz inside the models Ella (a, b), Billie (c, d), Louis (e, f), Glenn (g, h) and Fats (I, k) over all imaging positions. At the left column was investigated constant $B_1^+{}_{RMS}$ at the iso center of the coil and at the right column the limiting value of the global SAR was considered, Figure S2: Distribution of the magnitude of the tangential electrical field at 64 MHz inside the models Ella (a, b), Billie (c, d), Louis (e, f), Glenn (g, h) and Fats (I, k) over all coil configurations. At the left column was investigated constant $B_1^+{}_{RMS}$ at the iso center of the coil and at the right column the limiting value of the global SAR was considered, Figure S3: Distribution of the magnitude of the tangential electrical field at 128 MHz inside the models Ella (a, b), Billie (c, d), Louis (e, f), Glenn (g, h) and Fats (I, k) over all imaging positions. At the left column was investigated constant $B_1{}^+{}_{RMS}$ at the iso center of the coil and at the right column the limiting value of the global SAR was considered, Figure S4: Distribution of the magnitude of the tangential electrical field at 128 MHz inside the models Ella (a, b), Billie (c, d), Louis (e, f), Glenn (g, h) and Fats (I, k) over all coil configurations. At the left column was investigated constant $B_1{}^+{}_{RMS}$ at the iso center of the coil and at the right column the limiting value of the global SAR was considered, Table S1: Deviation in dB of the mean W value for different landmark positions. The coil was adjusted to generate $B_1{}^+{}_{RMS}$ =2μT at the iso center, Table S2: Deviation in dB of the mean W value for different landmark positions. The coil was adjusted to generate the limiting SAR value, Table S3: Deviation in dB of the mean W value for different coil configuration at landmark LD_3. The coil was adjusted to generate to generate $B_1{}^+{}_{RMS}$ =2μT at the iso center, Table S4: Deviation in dB of the mean W value for different coil configuration at landmark LD_3. The coil was adjusted to generate the limiting SAR value.

Author Contributions: Methodology, G.T.; Supervision, T.S. All authors have read and agreed to the published version of the manuscript.

Funding: This research received no external funding.

Institutional Review Board Statement: Not applicable.

Informed Consent Statement: Not applicable.

Data Availability Statement: Data is contained within the article or supplementary material.

Conflicts of Interest: Author George Tsanidis was employed by the company Thessaloniki Software Solutions (THESS) S.A. The remaining authors declare that the research was conducted in the absence of any commercial or financial relationships that could be construed as a potential conflict of interest.

References

1. Shellock, F.G.; Woods, T.O.; Crues, J.V. MR Labeling Information for Implants and Devices: Explanation of Terminology. *Radiology* **2009**, *253*, 26–30. [CrossRef] [PubMed]
2. Roguin, A.; Zviman, M.M.; Meininger, G.R.; Rodrigues, E.R.; Dickfeld, T.M.; Bluemke, D.A.; Lardo, A.; Berger, R.D.; Calkins, H.; Halperin, H.R. Modern Pacemaker and Implantable Cardioverter/Defibrillator Systems Can Be Magnetic Resonance Imaging Safe. *Circulation* **2004**, *110*, 475–482. [CrossRef] [PubMed]
3. Junttila, M.J.; Fishman, J.E.; Lopera, G.A.; Pattany, P.M.; Velazquez, D.L.; Williams, A.R.; Trachtenberg, B.H.; Sanina, C.; Mather, J.; Hare, J.M. Safety of Serial MRI in Patients with Implantable Cardioverter Defibrillators. *Heart* **2011**, *97*, 1852–1856. [CrossRef]
4. Rezai, A.R.; Baker, K.B.; Tkach, J.A.; Phillips, M.; Hrdlicka, G.; Sharan, A.D.; Nyenhuis, J.; Ruggieri, P.; Shellock, F.G.; Henderson, J. Is Magnetic Resonance Imaging Safe for Patients with Neurostimulation Systems Used for Deep Brain Stimulation? *Neurosurgery* **2005**, *57*, 1056–1062. [CrossRef]
5. Kalin, R.; Stanton, M.S. Current Clinical Issues for MRI Scanning of Pacemaker and Defibrillator Patients. *Pacing Clin. Electrophysiol.* **2005**, *28*, 326–328. [CrossRef] [PubMed]
6. Achenbach, S.; Moshage, W.; Diem, B.; Bieberlea, T.; Schibgilla, V.; Bachmann, K. Effects of Magnetic Resonance Imaging on Cardiac Pacemakers and Electrodes. *Am. Heart J.* **1997**, *134*, 467–473. [CrossRef] [PubMed]
7. Shellock, F.G.; Fieno, D.S.; Thomson, L.J.; Talavage, T.M.; Berman, D.S. Cardiac Pacemaker: In Vitro Assessment at 1.5 T. *Am. Heart J.* **2006**, *151*, 436–443. [CrossRef] [PubMed]
8. Luechinger, R.; Zeijlemaker, V.A.; Pedersen, E.M.; Mortensen, P.; Falk, E.; Duru, F.; Candinas, R.; Boesiger, P. In Vivo Heating of Pacemaker Leads during Magnetic Resonance Imaging. *Eur. Heart J.* **2004**, *26*, 376–383. [CrossRef]
9. Calcagnini, G.; Triventi, M.; Censi, F.; Mattei, E.; Bartolini, P.; Kainz, W.; Bassen, H.I. In Vitro Investigation of Pacemaker Lead Heating Induced by Magnetic Resonance Imaging: Role of Implant Geometry. *J. Magn. Reson. Imaging* **2008**, *28*, 879–886. [CrossRef]
10. Nordbeck, P.; Fidler, F.; Friedrich, M.T.; Weiss, I.; Warmuth, M.; Gensler, D.; Herold, V.; Geistert, W.; Jakob, P.M.; Ertl, G.; et al. Reducing RF-Related Heating of Cardiac Pacemaker Leads in MRI: Implementation and Experimental Verification of Practical Design Changes. *Magn. Reson. Med.* **2012**, *68*, 1963–1972. [CrossRef]
11. Langman, D.A.; Goldberg, I.B.; Judy, J.; Paul Finn, J.; Ennis, D.B. The Dependence of Radiofrequency Induced Pacemaker Lead Tip Heating on the Electrical Conductivity of the Medium at the Lead Tip. *Magn. Reson. Med.* **2011**, *68*, 606–613. [CrossRef] [PubMed]
12. Guerin, B.; Serano, P.; Iacono, M.I.; Herrington, T.M.; Widge, A.S.; Dougherty, D.D.; Bonmassar, G.; Angelone, L.M.; Wald, L.L. Realistic Modeling of Deep Brain Stimulation Implants for Electromagnetic MRI Safety Studies. *Phys. Med. Biol.* **2018**, *63*, 095015. [CrossRef] [PubMed]

13. Nordbeck, P.; Weiss, I.; Ehses, P.; Ritter, O.; Warmuth, M.; Fidler, F.; Herold, V.; Jakob, P.M.; Ladd, M.E.; Quick, H.H.; et al. Measuring RF-Induced Currents inside Implants: Impact of Device Configuration on MRI Safety of Cardiac Pacemaker Leads. *Magn. Reson. Med.* **2009**, *61*, 570–578. [CrossRef]
14. Nordbeck, P.; Ritter, O.; Weiss, I.; Warmuth, M.; Gensler, D.; Burkard, N.; Herold, V.; Jakob, P.M.; Ertl, G.; Ladd, M.E.; et al. Impact of Imaging Landmark on the Risk of MRI-Related Heating near Implanted Medical Devices like Cardiac Pacemaker Leads. *Magnetic Reson. Med.* **2010**, *65*, 44–50. [CrossRef] [PubMed]
15. Amjad, A.; Kamondetdacha, R.; Kildishev, A.V.; Park, S.M.; Nyenhuis, J.A. Power Deposition inside a Phantom for Testing of MRI Heating. *IEEE Trans. Magn.* **2005**, *41*, 4185–4187. [CrossRef]
16. Baker, K.B.; Tkach, J.A.; Phillips, M.D.; Rezai, A.R. Variability in RF-Induced Heating of a Deep Brain Stimulation Implant across MR Systems. *J. Magn. Reson. Imaging* **2006**, *24*, 1236–1242. [CrossRef]
17. Baker, K.B.; Tkach, J.A.; Nyenhuis, J.A.; Phillips, M.; Shellock, F.G.; Gonzalez-Martinez, J.; Rezai, A.R. Evaluation of Specific Absorption Rate as a Dosimeter of MRI-Related Implant Heating. *J. Magn. Reson. Imaging* **2004**, *20*, 315–320. [CrossRef] [PubMed]
18. Mattei, E.; Calcagnini, G.; Censi, F.; Triventi, M.; Bartolini, P. Numerical Model for Estimating RF-Induced Heating on a Pacemaker Implant during MRI: Experimental Validation. *IEEE Trans. Biomed. Eng.* **2010**, *57*, 2045–2052. [CrossRef]
19. Bhusal, B.; Elahi, B.; Keil, B.; Rosenow, J.M.; Kazemivalipour, E.; Golestanirad, L. Application of Surgical Lead Management and Reconfigurable Coil Technology to Reduce RF Heating of DBS Implants during MRI at 3T under Variant Body Compositions. *bioRxiv* **2020**. [CrossRef]
20. Bhusal, B.; Keil, B.; Rosenow, J.; Kazemivalipour, E.; Golestanirad, L. Patient's Body Composition Can Significantly Affect RF Power Deposition in the Tissue around DBS Implants: Ramifications for Lead Management Strategies and MRI Field-Shaping Techniques. *Phys. Med. Biol.* **2021**, *66*, 015008. [CrossRef]
21. Nguyen, B.T.; Pilitsis, J.G.; Golestanirad, L. The Effect of Simulation Strategies on Prediction of Power Deposition in the Tissue around Electronic Implants during Magnetic Resonance Imaging. *Phys. Med. Biol.* **2020**, *65*, 185007. [CrossRef]
22. Arduino, A.; Baruffaldi, F.; Bottauscio, O.; Chiampi, M.; Martinez, J.A.; Zanovello, U.; Zilberti, L. Computational Dosimetry in MRI in Presence of Hip, Knee or Shoulder Implants: Do We Need Accurate Surgery Models? *Phys. Med. Biol.* **2022**, *67*, 245022. [CrossRef]
23. Guo, R.; Zheng, J.; Chen, J. MRI RF-induced heating in heterogeneous human body with implantable medical device. In *High-Resolution Neuroimaging—Basic Physical Principles and Clinical Applications*; IntechOpen: London, UK, 2018. [CrossRef]
24. Nordbeck, P.; Fidler, F.; Weiss, I.; Warmuth, M.; Friedrich, M.T.; Ehses, P.; Geistert, W.; Ritter, O.; Jakob, P.M.; Ladd, M.E.; et al. Spatial Distribution of RF-Induced E-Fields and Implant Heating in MRI. *Magn. Reson. Med.* **2008**, *60*, 312–319. [CrossRef] [PubMed]
25. Murbach, M.; Cabot, E.; Neufeld, E.; Gosselin, M.-C.; Christ, A.; Pruessmann, K.P.; Kuster, N. Local SAR Enhancements in Anatomically Correct Children and Adult Models as a Function of Position within 1.5 T MR Body Coil. *Prog. Biophys. Mol. Biol.* **2011**, *107*, 428–433. [CrossRef] [PubMed]
26. Yao, A.; Murbach, M.; Goren, T.; Zastrow, E.; Kainz, W.; Kuster, N. Induced Radiofrequency Fields in Patients Undergoing MR Examinations: Insights for Risk Assessment. *Phys. Med. Biol.* **2021**, *66*, 185014. [CrossRef] [PubMed]
27. Mattei, E.; Triventi, M.; Calcagnini, G.; Censi, F.; Kainz, W.; Mendoza, G.; Bassen, H.I.; Bartolini, P. Complexity of MRI Induced Heating on Metallic Leads: Experimental Measurements of 374 Configurations. *BioMed. Eng. OnLine* **2008**, *7*, 11. [CrossRef]
28. Xia, M.; Zheng, J.; Yang, R.; Song, S.; Xu, J.; Liu, Q.; Kainz, W.; Long, S.A.; Chen, J. Effects of Patient Orientations, Landmark Positions, and Device Positions on the MRI RF-Induced Heating for Modular External Fixation Devices. *Magn. Reson. Med.* **2020**, *85*, 1669–1680. [CrossRef]
29. Golestanirad, L.; Kirsch, J.; Bonmassar, G.; Downs, S.; Elahi, B.; Martin, A.; Iacono, M.-I.; Angelone, L.M.; Keil, B.; Wald, L.L.; et al. RF-Induced Heating in Tissue near Bilateral DBS Implants during MRI at 1.5 T and 3T: The Role of Surgical Lead Management. *NeuroImage* **2019**, *184*, 566–576. [CrossRef]
30. Golestanirad, L.; Pilitsis, J.; Martin, A.; Larson, P.; Keil, B.; Bonmassar, G. (Eds.) Variation of RF heating around deep brain stimulation leads during 3.0 T MRI in fourteen patient-derived realistic lead models: The role of extracranial lead management. In Proceedings of the 25th Annual Meeting of the International Sosciety of Magnetic Resonance in Medicine, Honolulu, HI, USA, 22–27 April 2017.
31. Jiang, F.; Bhusal, B.; Nguyen, B.T.; Mongé, M.C.; Webster, G.; Kim, D.; Bonmassar, G.; Popsecu, A.R.; Golestanirad, L. Modifying the Trajectory of Epicardial Leads Can Substantially Reduce MRI-Induced RF Heating in Pediatric Patients with a Cardiac Implantable Electronic Device at 1.5T. *Magn. Reson. Med.* **2023**, *90*, 2510–2523. [CrossRef]
32. Jiang, F.; Bhusal, B.; Sanpitak, P.; Webster, G.; Popescu, A.; Kim, D.B. A comparative study of MRI-induced RF heating in pediatric and adult populations with epicardial and endocardial implantable electronic devices. In Proceedings of the 44th Annual International Conference of the IEEE Engineering in Medicine & Biology Society (EMBC), Glasgow, UK, 11–15 July 2022.
33. Ning, X.; Li, X.; Fan, X.; Chen, K.; Hua, W.; Liu, Z.; Dai, Y.; Chen, X.; Lu, M.; Zhao, S.; et al. 3.0 T Magnetic Resonance Imaging Scanning on Different Body Regions in Patients with Pacemakers. *J. Interv. Card. Electrophysiol.* **2020**, *61*, 545–550. [CrossRef]
34. Fagan, A.J.; Bitz, A.K.; Björkman-Burtscher, I.M.; Collins, C.M.; Kimbrell, V.; Raaijmakers, A.J.E. 7T MR Safety. *J. Magn. Reson. Imaging* **2020**, *53*, 333–346. [CrossRef] [PubMed]

35. Kazemivalipour, E.; Sadeghi-Tarakameh, A.; Keil, B.; Eryaman, Y.; Atalar, E.; Golestanirad, L. Effect of Field Strength on RF Power Deposition near Conductive Leads: A Simulation Study of SAR in DBS Lead Models during MRI at 1.5 T—10.5 T. *PLoS ONE* **2023**, *18*, e0280655. [CrossRef]
36. *IEC 60601-2-33*; Medical Electrical Equipment—Part 2–33: Particular Requirements for the Basic Safety and Essential Performance of Magnetic Resonance Equipment for Medical Diagnosis; Ed. 3.0. International Electrotechnical Commission: Geneva, Switzerland, 2010.
37. Nitz, W.R.; Brinker, G.; Diehl, D.; Frese, G. Specific Absorption Rate as a Poor Indicator of Magnetic Resonance-Related Implant Heating. *Investig. Radiol.* **2005**, *40*, 773–776. [CrossRef]
38. *ISO TS 10974_2018*; Assessment of the Safety of Magnetic Resonance Imaging for Patients with an Active Implantable Medical Device. International Organization for Standardization: Geneva, Switzerland, 2018.
39. Murbach, M.; Neufeld, E.; Kainz, W.; Pruessmann, K.P.; Kuster, N. Whole-Body and Local RF Absorption in Human Models as a Function of Anatomy and Position within 1.5T MR Body Coil. *Magn. Reson. Med.* **2013**, *71*, 839–845. [CrossRef]
40. Gosselin, M.-C.; Neufeld, E.; Moser, H.; Huber, E.; Farcito, S.; Gerber, L.; Jedensjö, M.; Hilber, I.; Gennaro, F.D.; Lloyd, B.; et al. Development of a New Generation of High-Resolution Anatomical Models for Medical Device Evaluation: The Virtual Population 3.0. *Phys. Med. Biol.* **2014**, *59*, 5287–5303. [CrossRef] [PubMed]
41. Hasgall, P.A.; Neufeld, E.; Gosselin, M.C.; Klingenböck, A.; Kuster, N. *IT'IS Database for Thermal and Electromagnetic Parameters of Biological Tissues Version 3.0*; ScienceOpen Inc.: Lexington, MA, USA, 2015.
42. Fischer, W.; Ritter, P. *Cardiac Pacing in Clinical Practice*; Springer Science & Business Media: Berlin/Heidelberg, Germany, 1998.
43. Park, S.-M.; Kamondetdacha, R.; Nyenhuis, J.A. Calculation of MRI-Induced Heating of an Implanted Medical Lead Wire with an Electric Field Transfer Function. *J. Magn. Reson. Imaging* **2007**, *26*, 1278–1285. [CrossRef]
44. Gudino, N.; Sonmez, M.; Yao, Z.; Baig, T.; Nielles-Vallespin, S.; Faranesh, A.Z.; Lederman, R.J.; Martens, M.; Balaban, R.S.; Hansen, M.S.; et al. Parallel Transmit Excitation at 1.5 T Based on the Minimization of a Driving Function for Device Heating. *Med. Phys.* **2014**, *42*, 359–371. [CrossRef]
45. Mattei, E.; Lucano, E. High Dielectric Material in MRI: Numerical Assessment of the Reduction of the Induced Local Power on Implanted Cardiac Leads. In Proceedings of the 38th Annual International Conference of the IEEE Engineering in Medicine and Biology Society (EMBC), Orlando, FL, USA, 16–20 August 2016. [CrossRef]
46. Bhusal, B.; Nguyen, B.T.; Vu, J.; Elahi, B.; Rosenow, J.M.; Nolt, M.J.; López-Rosado, R.; Pilitsis, J.G.; DiMarzio, M.; Golestanirad, L. The Effect of Device Configuration and Patient's Body Composition on Image Artifact and RF Heating of Deep Brain Stimulation Devices during MRI at 1.5T and 3T. *bioRxiv* **2020**. [CrossRef]
47. Golestanirad, L.; Rahsepar, A.A.; Kirsch, J.E.; Suwa, K.; Collins, J.C.; Angelone, L.M.; Keil, B.; Passman, R.S.; Bonmassar, G.; Serano, P.; et al. Changes in the Specific Absorption Rate (SAR) of Radiofrequency Energy in Patients with Retained Cardiac Leads during MRI at 1.5T and 3T. *Magn. Reson. Med.* **2018**, *81*, 653–669. [CrossRef]
48. Seo, Y.; Wang, Z.J. Measurement and Evaluation of Specific Absorption Rate and Temperature Elevation Caused by an Artificial Hip Joint during MRI Scanning. *Sci. Rep.* **2021**, *11*, 1134. [CrossRef]
49. Bottomley, P.A.; Edelstein, W.A.; Kumar, A.; Allen, J.M.; Karmarkar, P. Towards MRI-safe implanted leads: A comparative evaluation of four designs. In Proceedings of the International Society for Magnetic Resonance in Medicine, Stockholm, Sweden, 1–7 May 2010; Volume 18, p. 776.
50. Collins, C.M.; Smith, M.B. Calculations of B1 distribution, SNR, and SAR for a surface coil adjacent to an anatomically-accurate human body model. *Magn. Reason. Med.* **2001**, *45*, 692–699. [CrossRef]
51. Martinez, J.A.; Serano, P.; Ennis, D.B. Patient Orientation Affects Lead-Tip Heating of Cardiac Active Implantable Medical Devices during MRI. *Radiol. Cardiothorac. Imaging* **2019**, *1*, e190006. [CrossRef] [PubMed]
52. Zanchi, M.G.; Venook, R.; Pauly, J.M.; Scott, G.C. An Optically Coupled System for Quantitative Monitoring of MRI-Induced RF Currents into Long Conductors. *IEEE Trans. Med. Imaging* **2010**, *29*, 169–178. [CrossRef] [PubMed]
53. Overall, W.R.; Pauly, J.M.; Stang, P.P.; Scott, G.C. Ensuring Safety of Implanted Devices under MRI Using Reversed RF Polarization. *Magn. Reson. Med.* **2010**, *64*, 823–833. [CrossRef] [PubMed]
54. Zeng, Q.; Wang, Q.; Kainz, W.; Chen, J. Impact of RF Shimming on RF-Induced Heating near Implantable Medical Electrodes in a 3T MRI Coil. *IEEE Trans. Electromagn. Compat.* **2018**, *62*, 52–64. [CrossRef]
55. McElcheran, C.E.; Yang, B.; Anderson, K.J.T.; Golestanirad, L.; Graham, S.J. Parallel Radiofrequency Transmission at 3 Tesla to Improve Safety in Bilateral Implanted Wires in a Heterogeneous Model. *Magn. Reson. Med.* **2017**, *78*, 2406–2415. [CrossRef] [PubMed]
56. Lucano, E.; Liberti, M.; Lloyd, T.; Apollonio, F.; Wedan, S.; Kainz, W.; Angelone, L.M. A Numerical Investigation on the Effect of RF Coil Feed Variability on Global and Local Electromagnetic Field Exposure in Human Body Models at 64 MHz. *Magn. Reson. Med.* **2017**, *79*, 1135–1144. [CrossRef]
57. Zheng, J.; Lan, Q.; Kainz, W.; Long, S.A.; Chen, J. Genetic Algorithm Search for the Worst-Case MRI RF Exposure for a Multiconfiguration Implantable Fixation System Modeled Using Artificial Neural Networks. *Magn. Reson. Med.* **2020**, *84*, 2754–2764. [CrossRef]
58. Chen, X.; Zheng, C.; Golestanirad, L. Application of Machine Learning to Predict RF Heating of Cardiac Leads during Magnetic Resonance Imaging at 1.5 T and 3 T: A Simulation Study. *J. Magn. Reson.* **2023**, *349*, 107384. [CrossRef]

59. Chen, X.; Zheng, C.; Nguyen, B.T.; Sanpitak, P.; Chow, K.; Bi, X.; Elahi, B.; Golestanirad, L. Application of Deep Learning to Predict RF Heating of Cardiac Leads during Magnetic Resonance Imaging at 1.5 T and 3 T. *Res. Sq.* **2021**. [CrossRef]
60. Vu, J.; Nguyen, B.T.; Bhusal, B.; Baraboo, J.; Rosenow, J.; Bagci, U.; Bright, M.G.; Golestanirad, L. Machine Learning-Based Prediction of MRI-Induced Power Absorption in the Tissue in Patients with Simplified Deep Brain Stimulation Lead Models. *IEEE Trans. Electromagn. Compat.* **2021**, *63*, 1757–1766. [CrossRef] [PubMed]
61. Yao, A.; Zastrow, E.; Cabot, E.; Lloyd, B.; Schneider, B.; Kainz, W.; Kuster, N. Anatomical Model Uncertainty for RF Safety Evaluation of Metallic Implants under MRI Exposure. *Bioelectromagnetics* **2019**, *40*, 458–471. [CrossRef] [PubMed]